Internal load transfer in a metal matrix composite with a three-dimensional interpenetrating structure

S. Roy, J. Gibmeier, V. Kostov, Kay A. Weidenmann, A. Nagel, A. Wanner

Angaben zur Veröffentlichung / Publication details:

Roy, S., J. Gibmeier, V. Kostov, Kay A. Weidenmann, A. Nagel, and A. Wanner. 2011. "Internal load transfer in a metal matrix composite with a three-dimensional interpenetrating structure." *Acta Materialia* 59 (4): 1424–35. https://doi.org/10.1016/j.actamat.2010.11.004.

Internal load transfer in a metal matrix composite with a three-dimensional interpenetrating structure

S. Roy [a,*], J. Gibmeier [a], V. Kostov [a], K.A. Weidenmann [a], A. Nagel [b], A. Wanner [a]

[a] *Institut für Werkstoffkunde I, Karlsruher Institut für Technologie, 76128 Karlsruhe, Germany*
[b] *Hochschule Aalen, Beethovenstr. 1, 73430 Aalen, Germany*

1. Introduction

In a recent review article, Mortensen and Llorca [1] identified three main motivations behind the continued development of metal matrix composites (MMC). These are: (i) MMC allows one to go beyond the boundaries drawn by the properties of monolithic metals and ceramics [2], (ii) making a MMC is the only way of introducing a significant amount of an oxide or a carbide into an important metal; and (iii) incorporation of finely divided ceramics in metallic matrices allows the advantageous properties of the ceramic materials to be utilised. MMC can be classified according to the form of the reinforcement (e.g., fibres, particles, whiskers or short fibres, interpenetrating, etc.). Among these, MMC with an interpenetrating structure have been shown to have better strength, toughness and wear resistance in comparison with other composite structures [3,4]. Hence, much recent work has focused on the development and analysis of interpenetrating MMC with unique structures. These include MMC fabricated by reaction synthesis [5–7], by melt infiltration in wood ceramics [8], in three-dimensional (3-D) periodic preforms produced by robotic deposition [9], and in porous ceramic preforms fabricated by freeze-casting [10–12].

Several studies have used either neutron [13–16] or synchrotron X-ray [17–20] diffraction to study the internal load transfer mechanism in MMC. Both these techniques allow phase specific analysis to be carried out in the bulk of the material with different spatial resolutions. MMC with different reinforcement architecture have been studied so far. Particle reinforced MMC were studied by Daymond

* Corresponding author. Tel.: +49 721 608 2197; fax: +49 721 608 8044.
E-mail address: siddhartha.roy@kit.edu (S. Roy).

et al. [14] and Wanner and Dunand [18], short fibre reinforced MMC were studied by Garces et al. [13], while Maire et al. [21] studied the behaviour of unidirectional fibre reinforced MMC. In comparison, relatively limited studies have been carried out to analyse the load transfer mechanism in interpenetrating MMC with complex microstructures. Young et al. [20] studied the behaviour of interpenetrating composites with periodic 3-D structures, Wilkes et al. [19] studied the behaviour of MMC with an interpenetrating ceramic phase surrounding discrete metallic fibres, while Roy et al. [22] studied the behaviour of lamellar freeze-cast MMC. Owing to the experimental difficulty associated with large grain size (hence poor grain statistics) [20] and/or owing to the amorphous nature of one of the phases to X-rays [13], lattice strain evolution in only one of the phases of the MMC has mostly been studied. Furthermore, in most studies, only one or two diffraction planes of different phases were analysed.

In the present work, MMC with an interpenetrating structure was studied. It was fabricated by direct squeeze-casting AlSi12 melt in an open porous alumina preform. The preform was fabricated by pyrolysis of cellulose fibres used as pore-forming agent and subsequent sintering of alumina particles. The resulting preform had both micropores within the ceramic walls and macropores between those walls, which were infiltrated by the liquid metal. Following the nomenclature proposed by Newnham et al. [23], the studied material can be classified as having a 3–3 connectivity, with both phases forming interpenetrating 3-D networks. The MMC was subjected to external uniaxial compression and tension, while lattice microstrains in all three phases (alumina reinforcement, silicon and aluminium solid solution) along directions parallel and transverse to that of the applied load were measured using energy dispersive synchrotron X-ray diffraction (EDXRD). The lattice strain evolution in several (up to eight) diffraction planes of each phase was analysed, and in this way it was possible to gain insight into the elastic and elastic–plastic anisotropy of the individual phases. Moreover, analysis of multiple diffraction planes of each phase ensured that the calculated average microstrains and stresses were much more reliable and representative of the behaviour of the material in comparison with calculation using a single diffraction plane.

2. Experimental procedure

2.1. Specimen material

The composite material was fabricated by the Materials Research Team of Aalen University of Applied Sciences, Germany, following a processing route thoroughly described in Ref. [24]. Commercially available alumina powder (CL2500 from Almatis GmbH, Germany, with particle size 1.8 μm/$d50$ and nominal alumina content 99.8%) was used to prepare the porous ceramic performs, and 20 vol.% of cellulose fibres (Arbocel P290 from J. Rettenmaier & Söhne GmbH & Co. KG, Germany) with a nominal average length of 150 μm were added as a pore-forming agents. The alumina powder particles were first deglomerated by wet ball-milling, then they were mixed with the pore-forming agent and finally freeze-dried. The powders were pressed into plates with nominal dimensions $65 \times 45 \times 10$ mm^3 and then sintered in an electrically heated tube furnace under an oxidizing atmosphere. The sintering temperature was 1550 °C and, during this process, pyrolysis of the pore-forming agents also occurred. Fig. 1 shows a scanning electron microscopy (SEM) micrograph of the uninfiltrated ceramic preform with a nominal ceramic content of 41 vol.%. Several regions with traces of cellulose fibres can be observed in this image, and one such location is indicated by an arrow. The porous preforms were subsequently infiltrated with AlSi12 melt via direct squeeze-casting. Prior to squeeze-casting, the preform and the melt were preheated to 800 °C, while the tool was heated to 420 °C. An infiltration pressure of 100 MPa was applied.

2.2. Experimental procedure

EDXRD measurements were carried out at the Materials Science Beamline EDDI at the BESSY synchrotron source (Berlin, Germany). Schematic layout of the beamline components as well as the technical specifications can be found in Ref. [25], while a thorough description of the theoretical background of EDXRD can be found in Ref. [26]. Uniaxial tension and compression tests were carried out in situ using two different loading devices mounted alternately on the motorized diffractometer tables available at the EDDI experimental hutch. For the compression test, one sample with rectangular parallelepiped geometry was compressed between two hardened steel punches in a miniature mechanical testing machine manufactured by Kammrath & Weiss GmbH (Dortmund, Germany). Uniaxial tensile testing was carried out on a sample with a cylindrical cross section. A custom-made hydraulic tension/compression test set-up with a maximum load capacity of 20 kN, manufactured

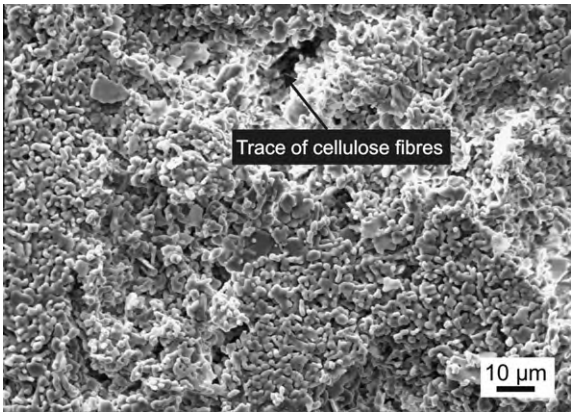

Fig. 1. SEM micrograph of the ceramic preform with nominal ceramic content of 41 vol.%.

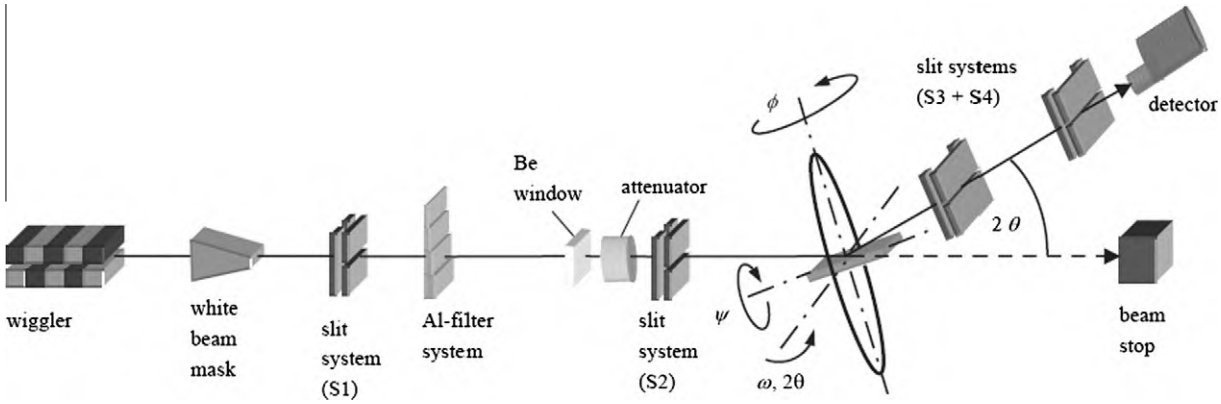

Fig. 2. Schematic layout of the EDDI beamline at BESSY [25].

by Walter + Bai AG (Löhningen, Switzerland) was used. External stress on the samples was increased stepwise and, at each stress step, the test was stopped, and diffraction measurements were carried out, following the $\sin^2\psi$ method [27] by stepwise tilting the test set-up at ψ between 0° and 90°. The diffraction experiments were carried out with a ω pre-tilt angle half that of the diffraction angle to align the scattering vector with the direction of load application. Definition of the ω angle can be found in the schematic layout of the beamline shown in Fig. 2. After each load application and before the corresponding diffraction measurement, sufficient waiting time (in the range 5–10 min) was maintained to minimize the effects of stress relaxation. The extent of stress relaxation was minimal in the macroscopic elastic region. However, it increased with the onset of plastic deformation in aluminium; reaching a value of ~12 MPa at the highest applied stress ($\sigma_{\max,\,\text{applied}} = 294$ MPa) in the tensile experiment. In both experiments, the slits in the path of the incoming beam had dimensions 1 × 1 mm, and the slits in the path of the transmitted beam had dimensions 60 μm × 5 mm. Individual diffraction lines from the EDXRD spectra were fitted by a "Pseudo-Voigt" function to determine the line positions. It is possible to determine lattice strains by calculating the shifts of the diffraction lines according to

$$\varepsilon = \frac{d^{hkl}}{d_0^{hkl}} - 1 = \frac{E_0^{hkl}}{E^{hkl}} - 1 \qquad (1)$$

where d_0^{hkl} and E_0^{hkl} are the lattice plane spacings and the energy peak positions of the $\{h\,k\,l\}$ family of planes in the unstressed condition, respectively.

2.2.1. Compression test

A detailed description of the experimental procedure for the in situ compression test along with a photograph of the compression test set-up mounted on the diffraction table can be found in an earlier publication [22], and only a brief description is given here. The sample had the shape of a rectangular parallelepiped, with nominal dimensions 2.29 × 2.43 × 2.50 mm^3. Commercially available aluminium foils 20 μm thick were used between the sample and the steel punches to reduce internal friction during compression. The diffractometer unit had a θ–θ diffractometer, which was further equipped with a five-axis sample positioning unit and a detector arm with two slit systems to define the diffracted beam. This experimental set-up is suitable for relatively small and lightweight sample environments weighing up to 3 kg [25]. A scattering angle $2\theta = 7°$ was chosen, as it gave good energy separation as well as sufficient peak intensities. A gauge volume with nominal volume of 0.12 mm^3 was defined by the primary and secondary slits. A preload in the range of 30 N (corresponding to a compressive stress of ~5 MPa) was first applied to ensure that the sample did not fall down during subsequent measurement. Lattice spacing with only this preload was used as the initial value for further calculations. Hence, the processing-induced thermal residual stresses were ignored as a first approach, and only the extent of internal load transfer under an applied external stress was measured. As lattice spacing with only the applied preload was used as the basis for strain calculation, reported strains are the changes with respect to this initial state. From here on, only "strain" will be used to denote this change in lattice strain. The load steps followed during the compression test are shown in Fig. 3.

2.2.2. Tension test

The tensile sample had a 10-mm uniform gauge length in the middle and a 5-mm gauge diameter. Because of the heavier weight of the tensile testing rig compared with the Kammrath & Weiss device used for the compression test, a second diffractometer unit was used in this case. This unit consisted of a four-axis sample positioner mounted on a basic y–z stage, and it could carry a maximum of 30 kg. A detailed description of the set-up can be found in Ref. [25]. The slits in the path of the incoming and the diffracted beam had the same dimensions as in the compression test; however, owing to the different experimental set-up, the scattering angle was different. A scattering angle $2\theta = 10.27°$ was chosen. This diffraction angle resulted from the design constraints of the second diffractometer unit used for the experiment. This resulted in a gauge volume with a

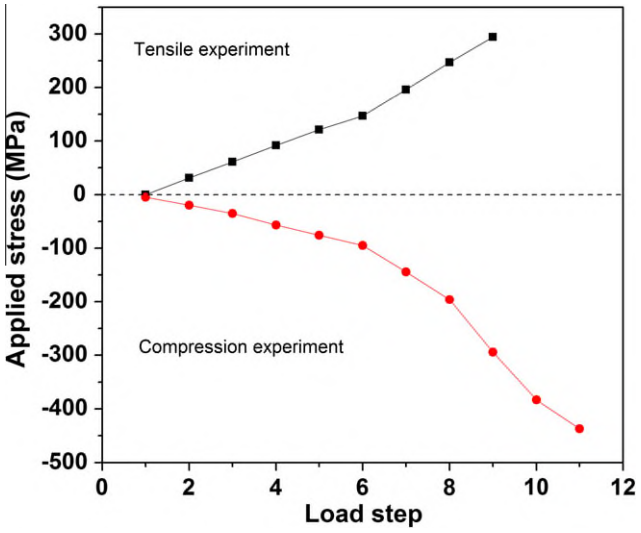

Fig. 3. Loading history of the two samples.

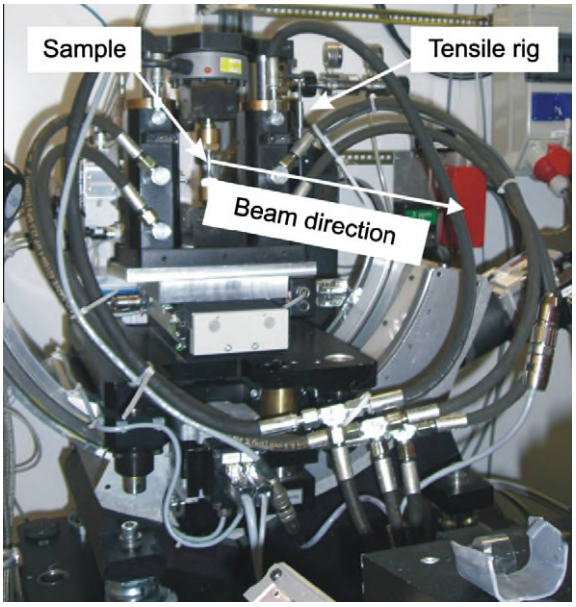

Fig. 4. Photograph of the tensile test set-up mounted on the diffraction table at EDDI beamline at BESSY, Berlin. The actual sample is shown marked in the photograph.

nominal value of 0.3 mm^3 defined by the primary and the secondary slits. In the schematic layout of the beamline set-up shown in Fig. 2, only the location of the sample positioning table with respect to other components of the beamline can be observed. A closer view of the sample positioning table along with the tensile testing rig used in the present study is shown in Fig. 4. It also shows the actual tensile testing specimen mounted between the two crossheads. Similarly, in the compression test, the first measured lattice spacing was used as the initial value for further calculations. The load steps followed during tensile experiment are shown in Fig. 3.

3. Experimental results

3.1. Microstructure

Fig. 5 shows typical cross sections of the MMC for the face perpendicular to the direction of squeeze-casting. Fig. 5a shows a light optical micrograph, while Fig. 5b shows a SEM micrograph. The optical micrograph shows clusters rich in alumina, while the regions away from the clusters are rich in the AlSi12 matrix alloy. The SEM image shows that these alumina-rich regions are not densely packed. Instead, they are composed of individual alumina particles with metallic matrix between them. The structure results directly from the structure of the ceramic preform. As the preform was fabricated by simultaneous pyrolysis of the pore-forming agents and sintering of the green powder compact, it had both micropores within the ceramic walls in the preform and macropores between those walls. These pores were filled by the metallic alloy during melt infiltration to generate the interpenetrating structure. The optical micrograph also reveals the dendritic structure of the cast aluminium solid solution, and silicon particles are randomly distributed within them. These silicon particles are mostly rod shaped, with aspect ratios in the range

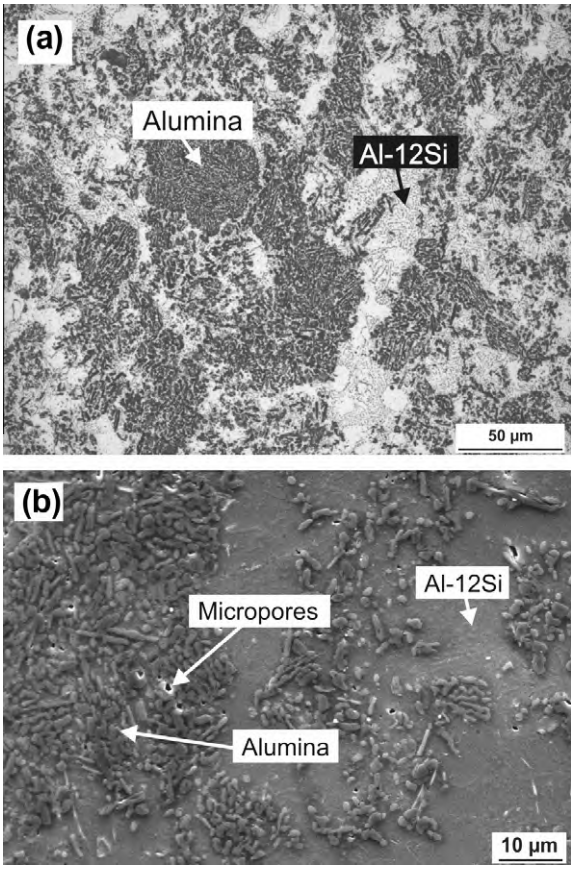

Fig. 5. Micrographs of the studied composite material: (a) light optical micrograph and (b) SEM micrograph.

10–50. No trace of residual porosity can be observed in the optical micrograph. The SEM image, however, reveals the

presence of some very small submicron pores, which were not properly infiltrated. The densities of the MMC samples studied were measured using a high-precision laboratory balance with a standard deviation of 5×10^{-5}%. For the sample undergoing compression, the density was measured from its mass and dimensions, and it was found to be 3.019 Mg m^{-3}. For the tensile sample, the density was measured according to Archimedes' principle by immersing the sample in distilled water, and it was found to be 3.146 Mg m^{-3}. Neglecting porosity and using the bulk densities of alumina and AlSi12 (the density of alumina was taken as 3.90 Mg m^{-3} [28], while the density of AlSi12 was measured in an earlier study as 2.63 Mg m^{-3} [29]), the ceramic contents in the compressive and tensile samples were found to be 31 vol.% and 41 vol.%, respectively. The two samples were machined from different MMC plates, and the large difference in their ceramic content may be attributed to this. However, the presence of porosity may lead to a deviation in the calculated ceramic volume content in the two MMC samples. In their study on the diamond reinforced Al-alloy MMC, Weidenmann et al. [30] attributed the residual porosity in the MMC to stronger shrinkage of the matrix than the ceramic particles during cooling from solidification temperature, and to incomplete infiltration owing to insufficient infiltration pressure. As 100 MPa pressure was applied during squeeze-casting to fabricate the MMC in the present study, porosity resulting from insufficient applied pressure can be neglected. Following this approach, the amount of residual porosity in the studied MMC samples was estimated to lie in the range 0.3–0.4 vol.%. This may shift the calculated alumina content in the two samples to a value ~0.7 vol.% higher than that, assuming no porosity.

3.2. Raw data analysis from EDXRD

Fig. 6 shows typical EDXRD spectra for the MMC samples studied. The spectrum marked "a" corresponds to the sample tested under compression at a diffraction angle $2\theta = 7°$, while the spectrum marked "b" denotes the sample tested under tension using a diffraction angle $2\theta = 10.27°$. Following Ref. [26], an increase in 2θ shifts the complete diffraction pattern to lower energy levels in the plot marked "b". For the compression sample, eight diffraction planes of alumina, four diffraction planes of Al, and three diffraction planes of Si were analysed; while for the tensile sample, seven diffraction planes of alumina, four diffraction planes of Al, and two diffraction planes of Si were studied. Fig. 7 shows representative d vs. $\sin^2\psi$ plots for the {3 1 1} family of planes for Al, {1 1 3} family of planes for alumina and {1 1 1} family of planes of Si. Plots for only the sample undergoing compression are shown here, while the plots for the sample undergoing tension exhibited similar trends. Each plot in Fig. 7 contains data for all applied stresses. The lines shown in the plot are the best fit lines over the complete $\sin^2\psi$ range. In each plot, the point corresponding to $\sin^2\psi = 0$ is marked

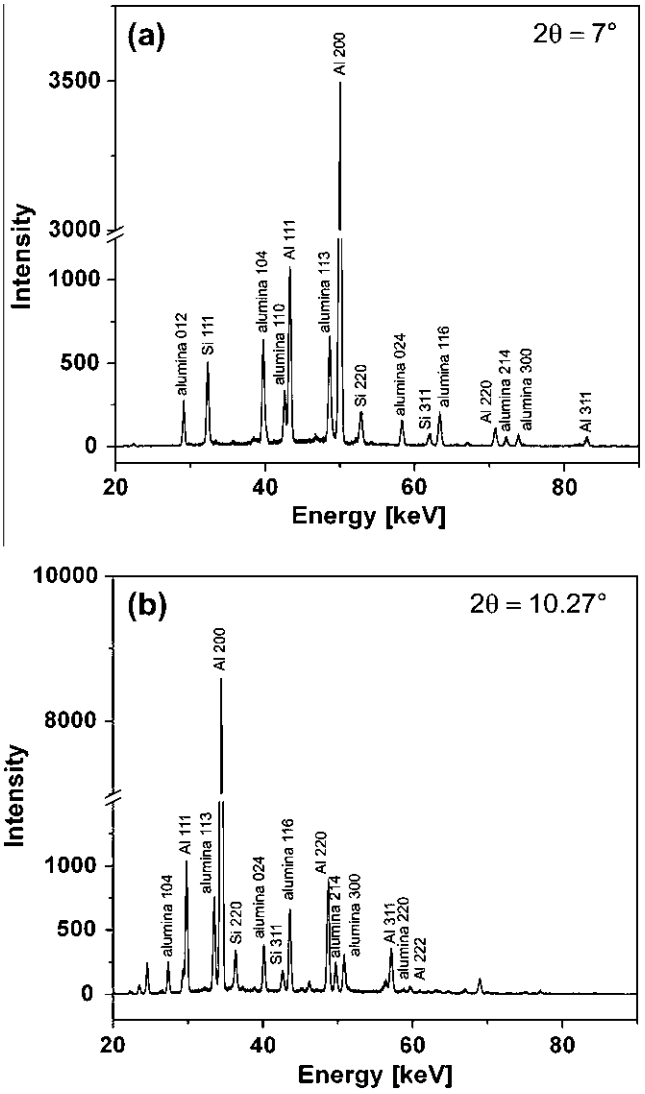

Fig. 6. Typical EDXRD spectra for the sample tested under (a) compression and (b) tension. Indexed diffraction planes of each phase are marked in each spectrum.

"transverse", while the point corresponding to $\sin^2\psi = 1$ is marked "parallel". This is due to the fact that, for the sample undergoing compression, at $2\theta = 7°$, the diffraction vector (and hence the direction of strain measurement) was transverse to the loading direction for $\sin^2\psi = 0$, while the diffraction vector was parallel to the loading direction for $\sin^2\psi = 1$. At each applied stress, the d vs. $\sin^2\psi$ plots were fitted with a straight line. Subsequently, the d-spacings at $\sin^2\psi = 1$ and at $\sin^2\psi = 0$ were determined from this best fit line, and they were used as the d-spacings along and transverse to the loading direction, respectively. For the tensile sample, the loading direction was orthogonal to the compression test based on the design of the loading devices. Hence, the diffraction vector was parallel to the loading direction at $\sin^2\psi = 0$, while it was transverse to the loading direction at $\sin^2\psi = 1$. Hence, in this case the d-spacings at $\sin^2\psi = 0$ and at $\sin^2\psi = 1$ were determined from the best fit lines, and they were used as the d-spacings along and transverse to the loading direction, respectively.

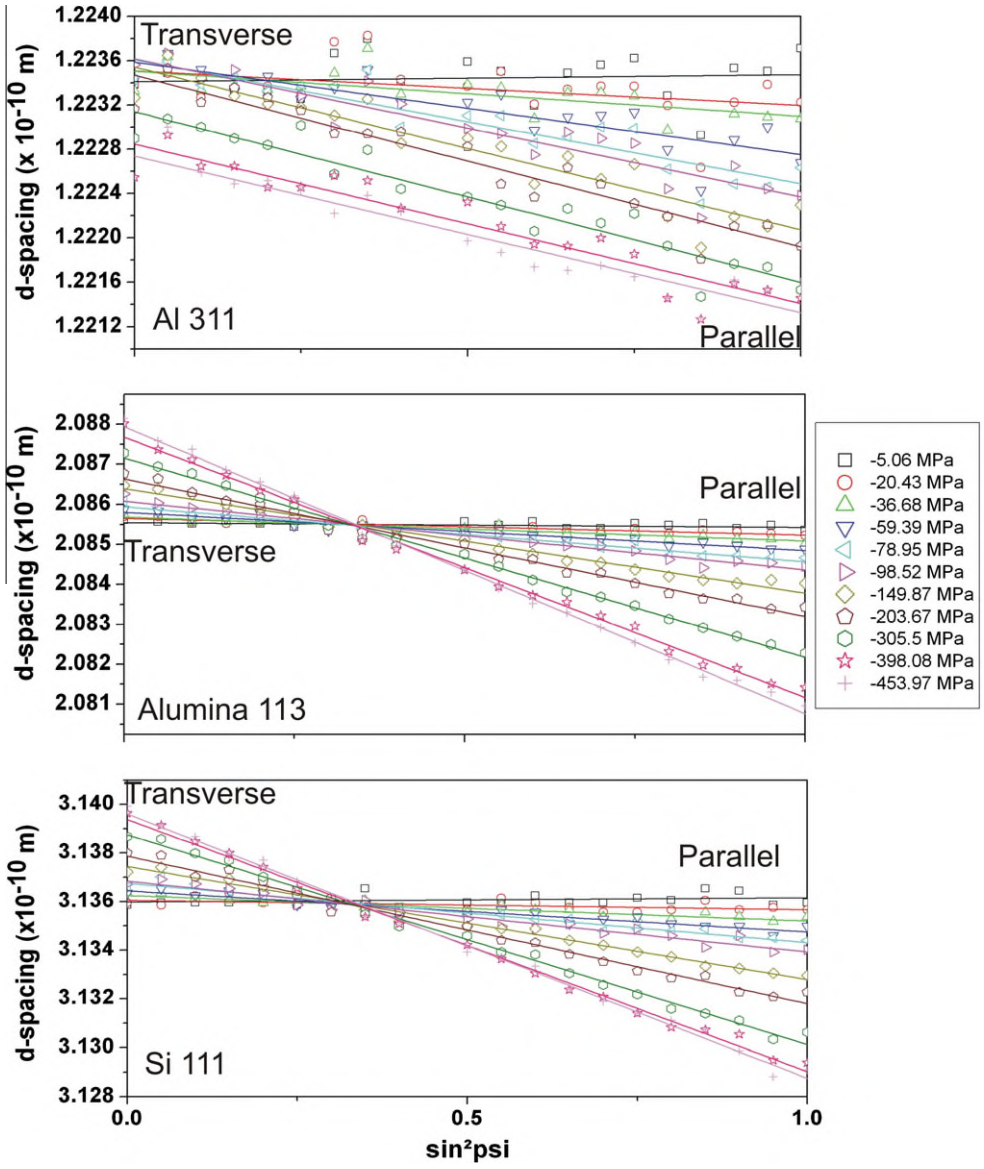

Fig. 7. Plots of lattice spacing (in 10^{-10} m) vs. $\sin^2\psi$ at all applied stresses for the sample undergoing compression. Representative plots for {3 1 1} family of planes of Al, {1 1 3} family of planes of alumina and {1 1 1} family of planes of Si are shown.

3.3. In situ compression and tension tests by EDXRD

Figs. 8 and 10 show the evolution of the lattice microstrain along the loading direction in all three phases of the MMC as a function of externally applied compressive and tensile stress, respectively. In both figures, plots "a–c" show the microstrains in all indexed planes of each phase as well as the continuum mechanics equivalent elastic microstrain computed therefrom. The continuum mechanics equivalent elastic microstrain was computed following the methodology described by Daymond [31], using the multiplicity factor of each diffraction plane and assuming absence of crystallographic texture (i.e., the texture factor was taken as unity) as a first approach. Figs. 8d and 10d show the continuum mechanics equivalent elastic strain in all three phases as a function of applied stress. Figs. 9 and 11 show the evolution of transverse lattice microstrain as a function of externally applied compressive and tensile stress, respectively. In these figures, the microstrain evolution in individual diffraction planes has not been shown for the sake of clarity. In all the figures, the error bars correspond to the standard deviation of the lattice microstrains among all the indexed diffraction planes of each phase, and they mirror to some extent the effect of interplanar anisotropy.

4. Discussion

4.1. d vs. $\sin^2\psi$ plots

Fig. 7 shows that the best fit lines of the d vs. $\sin^2\psi$ plots for alumina and silicon at all applied stresses pass through

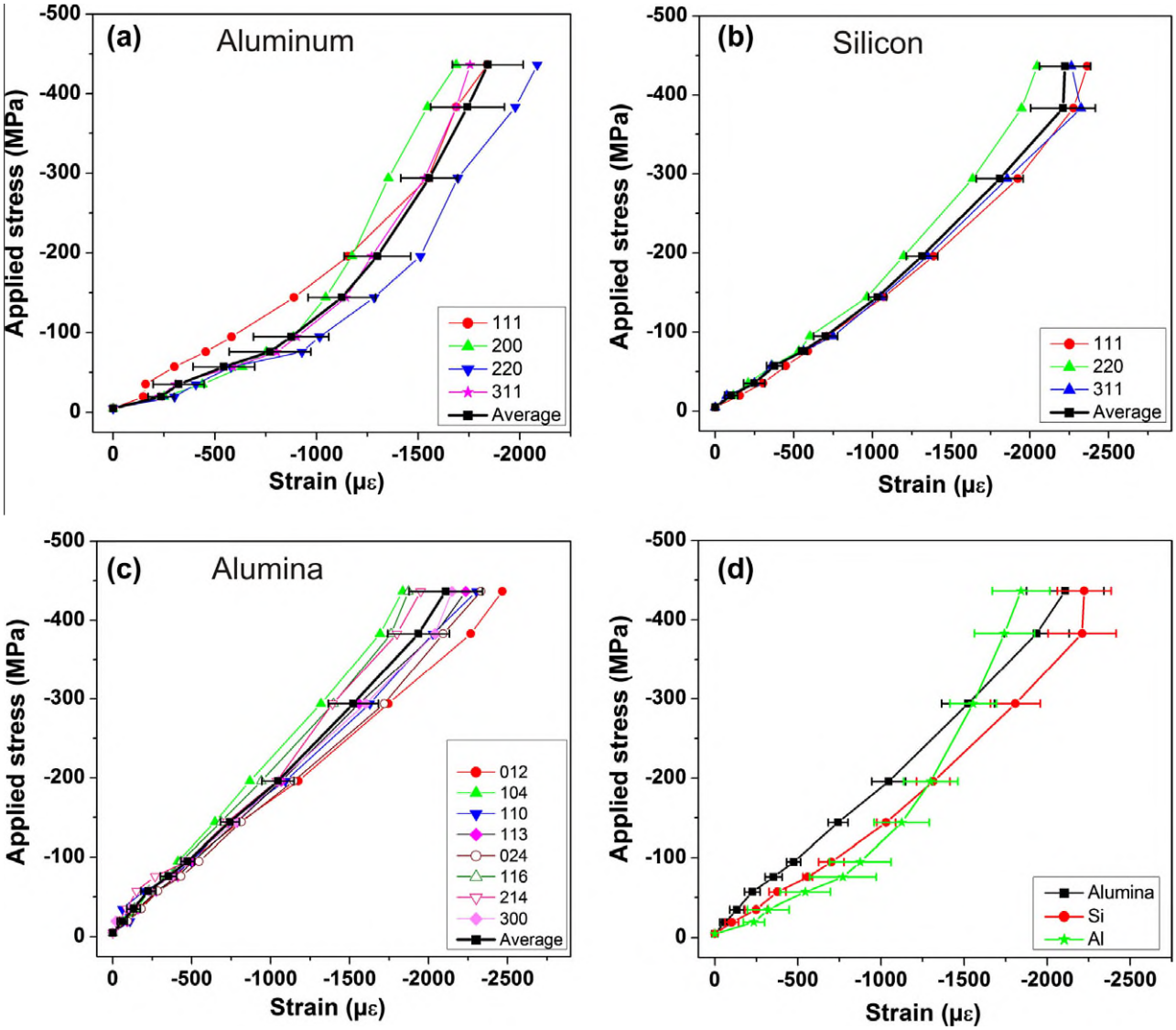

Fig. 8. Evolution of lattice microstrain along the loading direction as a function of applied compressive stress: (a) Al, (b) Si, (c) alumina and (d) combined plot showing the phase specific continuum mechanics equivalent behaviour.

or close to one single point. This point can be used as the strain independent lattice spacing for the respective phases [32]. Furthermore, as expected, the slopes of the lines for alumina and silicon progressively increase at higher applied stresses. However, in aluminium, the best fit lines pass through one point only up to an applied stress of -100 MPa, and subsequently at higher stresses they lie parallel, without intersecting each other. The slopes of the d vs. $\sin^2\psi$ plots are proportional to the deviatoric stress component. Once aluminium starts to deform plastically, it transfers the load to the stiffer phases, and so the deviatoric stress remains almost constant. Hence, the best fit lines for aluminium in the plastic region show similar slope, while their slope increases in alumina and silicon. The extreme scatter in the data points of aluminium may be attributed to preferred orientation (large grain size and texture).

4.2. Evolution of lattice microstrain

Fig. 8 shows that under an applied compressive stress, the lattice microstrains in all three phases initially increase with increasing stress, suggesting that all phases are behaving in an elastic manner. At applied stresses more than ~ -100 MPa, the slope of the plot of aluminium changes abruptly and shows an upward trend. This denotes the point of initiation of plastic deformation within aluminium, whereupon the mismatch between the elastically and plastically deforming phases increases and, subsequently, a higher fraction of load is carried by the stiffer alumina and silicon phases. Simultaneously, the plots of alumina and silicon show an outward trend to maintain the stress balance. At applied stresses > -380 MPa, the slope of silicon changes to vertical, and that of alumina also shows an upward trend. This suggests that relaxation is occurring within silicon and

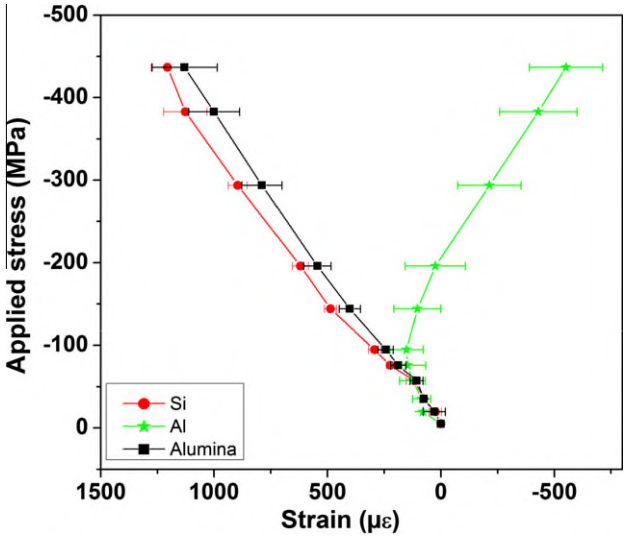

Fig. 9. Evolution of continuum mechanics equivalent transverse lattice microstrain as a function of applied compressive stress in all three phases.

alumina at this point. As both silicon and alumina are brittle, this relaxation may be attributed to the cracking of both these phases. Fig. 10 shows the evolution of lattice microstrains in all three phases along the loading direction when loaded under tension. Qualitatively, the behaviour is similar to that observed in Fig. 8. However, the sample was loaded to only ~300 MPa, and hence relaxation mechanisms were not observed within silicon and alumina.

If significant thermal residual stresses are present within the MMC, they may cause a matrix yield point mismatch between tension and compression. As the thermal expansion coefficient of the metallic matrix is almost always higher than the ceramic, thermal residual stresses should be tensile in the matrix, and they should be compressive in the ceramic. Subsequently, this may lead to higher in situ yield strength of the matrix and/or MMC in compression than in tension [33]. In both Figs. 8d and 10d, in the plots of aluminium the slope change occurs (initiation of plastic deformation) at absolute applied stresses of ~100 MPa. Hence, it is assumed that processing-induced thermal residual stress does not play a significant role.

A more direct estimate of the plastic deformation and strain hardening in aluminium is the evolution of the diffraction peak width of aluminium as a function of applied stress. As an example, Fig. 12 shows the evolution of the diffraction peak width of {1 1 1} planes in aluminium as a function of applied compressive stress. Other diffraction planes of aluminium showed a similar trend. At any applied stress, the average of the peak widths at all Ψ tilts was taken as the peak width, and the standard deviations of the peak widths at all tilts at a particular stress are shown as error bars. A similar trend, although less conclusively, could also be observed in the sample undergoing tensile experiment. Fig. 12 clearly shows that, up to an applied stress of ~−100 MPa the diffraction peak widths remain relatively constant. At higher compressive stresses, owing to the generation of dislocations during plastic deformation and their elastic interaction with the obstacles within the microstructure (e.g., dislocations), the diffraction peak width increases with increasing stress.

Figs. 9 and 11 show the evolution of the transverse lattice microstrains in all three phases as a function of applied stress. In both figures, initially the signs of the microstrains in all phases are opposite to those along the loading path. This is due to the Poisson effect. The transverse microstrain evolution in aluminium is complex. In both samples, up to an absolute applied stress of ~100 MPa, the trend shown by it is similar to those shown by alumina and silicon. However, at higher stresses, its behaviour changes; the microstrains become progressively compressive in the sample studied under compression, and vice versa. This is due to the sudden change in the Poisson ratio of aluminium from ~0.3 in the elastic state to 0.5 during plastic deformation. Poisson's ratio of alumina remains at its elastic value of 0.24 [34]. Owing to this, the transverse microstrain evolution in aluminium is constrained by stiffer and stronger alumina, and this causes the observed effect in aluminium.

The negative ratio of the slopes of the best fit straight lines in the plot of alumina in Figs. 8d and 9 is 0.52. This ratio is 0.20 when Figs. 10d and 11 are considered. The proximity of this ratio in the tensile sample with the Poisson's ratio of pure alumina (=0.24) suggests that the average stress state in alumina in this sample is close to uniaxial. The much higher value obtained in the compression test may be attributed to the barrelling effect. Barrelling typically occurs under compressive loading of a sample with length/diameter ratio <2.0 and in the presence of frictional forces at the contact points between the sample and the punches applying the load [35]. The length/thickness ratio of the sample undergoing compression test was ~1, and although 20-μm-thick Al foils were used between the sample and the punches in order to reduce the effect of friction, the remaining frictional forces might have resulted in non-negligible amount of barrelling.

4.3. Interplanar anisotropy

The evolution of lattice microstrain in several diffraction planes of each phase is shown in Figs. 8a–c and 10a–c. Variations in lattice strain among different diffraction planes of a single phase are due to interplanar anisotropy. When all three phases behave elastically, only a slight variation among microstrains in different planes of silicon is observed. However, once aluminium starts to deform plastically, in both samples, the microstrain evolution in the {2 2 0} planes of silicon show an upward trend. This suggests that, once load transfer starts to take place owing to plastic deformation of aluminium, the silicon grains with {2 2 0} orientation carry less load. The interplanar anisotropy in alumina in the elastic region is also very weak. However, in the plastic region of aluminium, the family of planes of alumina with {1 0 4} orientation tend to behave as the stiffest. For the sample undergoing compression, evolution of the lattice microstrain in planes with

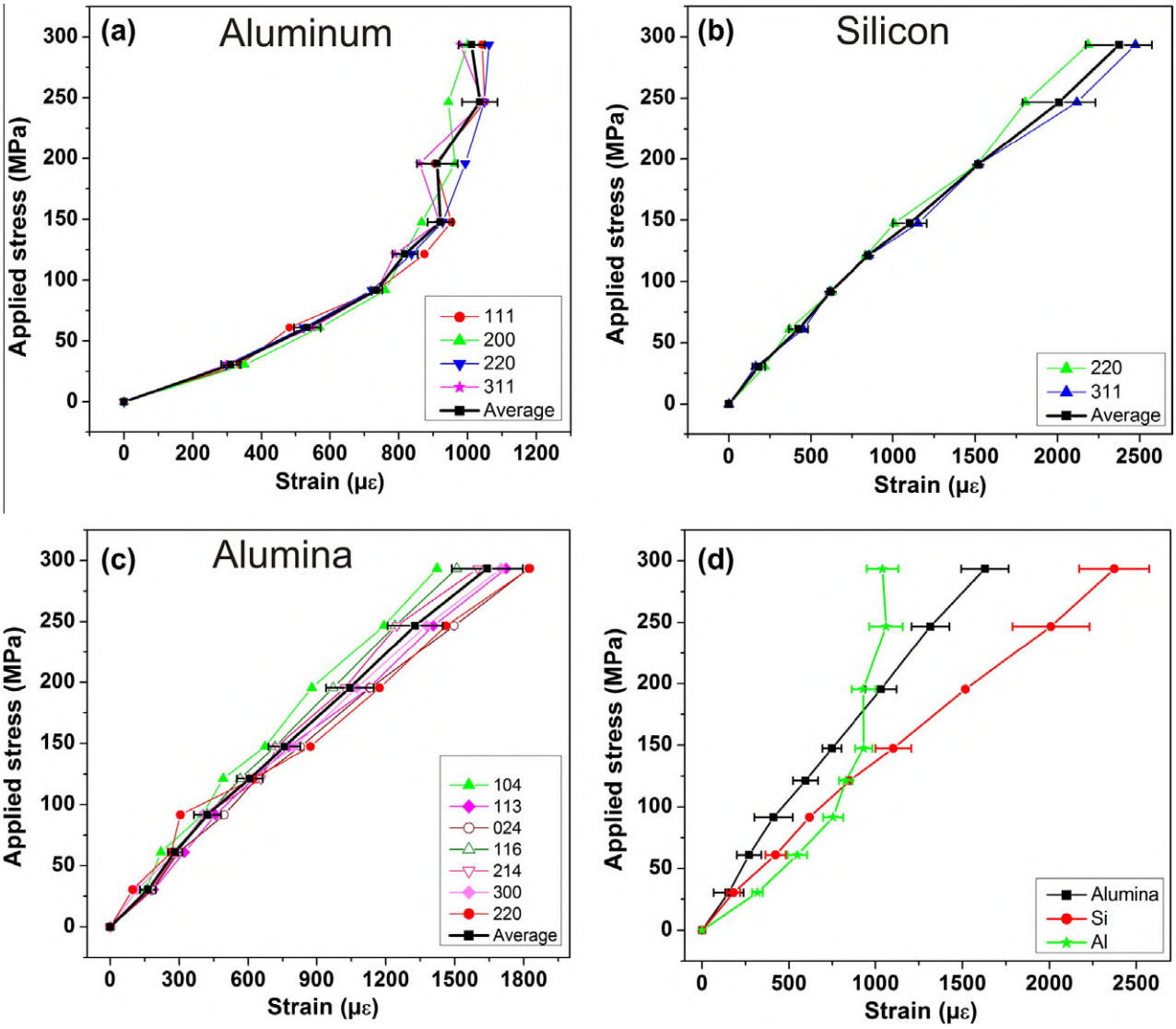

Fig. 10. Evolution of lattice microstrain along the loading direction as a function of applied tensile stress: (a) Al, (b) Si, (c) alumina and (d) combined plot showing the phase specific continuum mechanics equivalent behaviour.

{0 1 2} and {0 2 4} orientation in alumina is almost similar. This is expected, as these planes are equivalent. The average difference in strain response within these two planes at all stresses is 53 microstrains, and this may be interpreted as the error associated with the technique. In the aluminium phase of the sample undergoing compression, {1 1 1} planes are the stiffest in the elastic range. However, once plastic deformation starts, these planes behave as one of the most compliant, and the {2 0 0} planes, which are among the most compliant in the elastic deformation region, behave much more stiffly. A similar trend for aluminium has also been predicted by Clausen et al. [36].

4.4. Calculation of longitudinal phase stress and stress concentration factor

Average phase stress along the loading direction (referred to as longitudinal phase stress from here on) can be calculated from the measured longitudinal and transverse elastic lattice strains following the equation [37]

$$\sigma_1 = \frac{E}{1+v}\cdot\varepsilon_1 + \frac{v\cdot E}{(1+v)\cdot(1-2v)}\cdot(\varepsilon_1+\varepsilon_2+\varepsilon_3) \quad (2)$$

In this equation, σ_1 is the calculated longitudinal phase stress, ε_1 is the average lattice microstrain in each phase along the loading direction, $\varepsilon_2 = \varepsilon_3$ are the average lattice microstrains in each phase along transverse directions, and E and v are the E modulus and Poisson's ratio, respectively. The macroscopic E modulus and Poisson's ratio of each phase have been taken as E and v. Eq. (2) is based on the assumption that the individual phases of the composite are elastically isotropic. In alumina, the elastic anisotropy is relatively small [38], and the strains measured from several diffraction planes (eight diffraction planes for the compression test, and seven diffraction planes for the tensile test) were used to calculate the average lattice

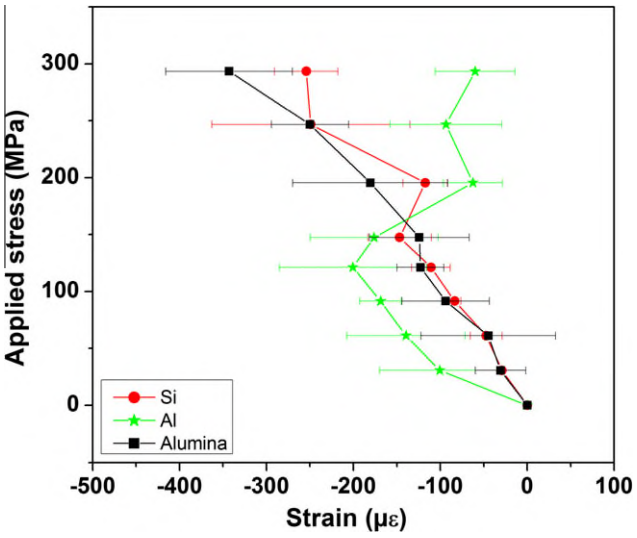

Fig. 11. Evolution of continuum mechanics equivalent transverse lattice microstrain as a function of applied tensile stress in all three phases.

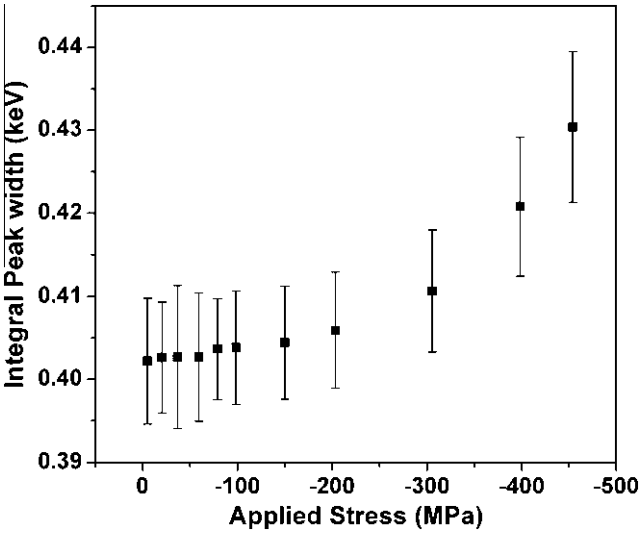

Fig. 12. Diffraction peak width as a function of external compressive stress for the {1 1 1} family of planes of aluminium.

strains. In aluminium in the elastic region, the assumption of isotropy is also justified, as the elastic anisotropy is also small in aluminium (aluminium has a single crystal cubic anisotropy ratio $(C_{11}-C_{12})/2C_{44}=0.82$ [39]). Among the three phases of the MMC, the elastic anisotropy is largest in silicon (it has a single crystal cubic anisotropy ratio $(C_{11}-C_{12})/2C_{44}=0.64$ [40]). In addition, average strains in silicon were calculated from strains measured from only three diffraction planes for the sample in compression and from only two diffraction planes for the sample in tension. Therefore, the assumption of elastic isotropy may cause significant errors in the calculated longitudinal stress in silicon.

Fig. 13 shows the calculated longitudinal stress in each phase plotted against the applied stress under compression

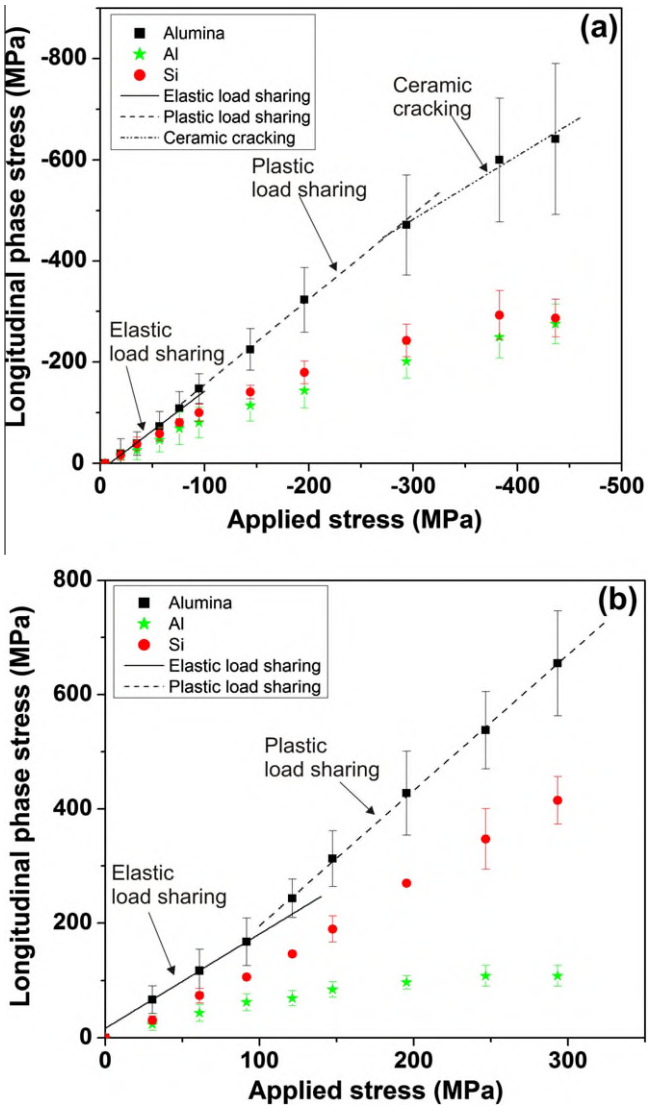

Fig. 13. Plot of longitudinal phase stress vs. applied stress for the sample undergoing: (a) compression and (b) tension. Black lines denote the best fit lines for the alumina phase in the intervals of elastic load sharing, plastic load sharing and ceramic cracking.

(Fig. 13a) and tension (Fig. 13b), respectively. Error bars in these plots correspond to the standard deviation in the stress calculation resulting from interplanar anisotropy. In each plot, best fit straight lines for alumina at different intervals of applied stress are shown by black lines. Three straight lines with different slopes can be observed for the sample undergoing compression. Elastic load sharing is observed up to ~ -100 MPa. At higher stresses, the slope of the best fit line slightly increases, suggesting plastic load transfer from aluminium, and finally, at stresses higher than ~ -300 MPa, the slope of the best fit line again decreases, suggesting initiation of damage. Only two such intervals can be observed in the plot of alumina in the sample undergoing tension. Elastic load sharing is again observed up to $|\sigma_a| \approx 100$ MPa, and at higher stresses the slope of the best fit line increases, suggesting increased load transfer owing to plastic deformation of aluminium. No

damage could be identified in this sample by means of the diffraction data.

The ratio of the longitudinal phase stress and the applied stress may be defined as the phase stress concentration factor. Fig. 14 shows this stress concentration factor in each phase plotted against the applied stress under external compression (Fig. 14a) and tension (Fig. 14b), respectively. Error bars in these plots correspond to the ratio of the standard deviation in stress calculation owing to interplanar anisotropy and the applied stress. In aluminium, in both samples, the stress concentration factor is less than unity, and it decreases with increasing applied stress, suggesting load transfer to stiffer and stronger silicon and alumina phases. The maximum stress concentration factor in silicon is marginally higher than unity in the sample under compression. At higher stresses, it decreases owing to cracking of the silicon particles. In contrast, the stress concentration factor in silicon increases continuously in the tensile sample. Fig. 14a shows that, in the sample under compression, the stress concentration factor in silicon already starts to decrease at applied stresses slightly higher than −100 MPa. However, Fig. 8b shows that the average lattice strain in silicon increases with applied stress up to an applied stress of −380 MPa. This difference between these two plots may arise as a result of barrelling of this sample during compression. Owing to this phenomenon, the measured transverse lattice strains were significantly higher in comparison with the tensile sample. Subsequently, following Eq. (2), an increase in the measured transverse lattice strain reduces the calculated longitudinal phase stress. In alumina, in the sample under compression, the stress concentration factor reaches a maximum value of ∼1.7 in the region marked with plastic load sharing. At applied stresses >−300 MPa, the stress concentration factor in alumina decreases owing to damage of the ceramic. The maximum stress concentration factor in alumina in the sample under external tension is ∼2.2, suggesting that for the same applied stress, the longitudinal stress in alumina in this sample is significantly higher than in the sample under compression. This may be attributed to the higher alumina content in the tensile sample and reduction of the longitudinal phase stress in the compressive sample owing to an increase in transverse lattice strains resulting from barrelling.

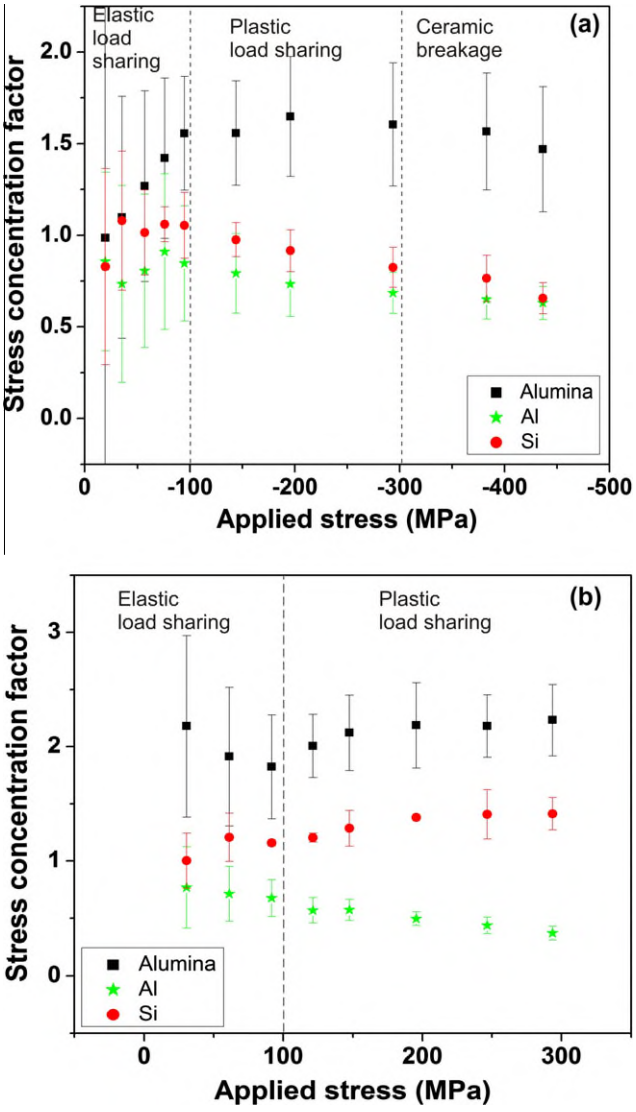

Fig. 14. Stress concentration factors in individual phases as a function of applied external: (a) compressive and (b) tensile stress. Regions of elastic and plastic load sharing and ceramic breakage are separated by dotted lines.

5. Conclusions

Internal load transfer under externally applied tension and compression in a three-dimensionally interpenetrating MMC was studied in this work. The MMC was produced by squeeze-casting AlSi12 melt in porous alumina preforms. The preforms were fabricated by pyrolysis of cellulose fibres used as a pore-forming agent and subsequent sintering of alumina particles. EDXRD is shown to be a powerful tool for this purpose. Measurements were carried out in transmission mode at different applied stresses according to the $\sin^2\psi$ method of X-ray stress analysis. Multiple diffraction peaks in all phases of the composite were analysed. This allowed information about the interplanar anisotropy of the different phases to be obtained. Under external stress, load transfer takes place from the softer and more compliant aluminium matrix to the stiffer and stronger silicon and alumina phases. Longitudinal stresses and stress concentration factors in all three phases were calculated from the measured continuum mechanics equivalent lattice strains and the macroscopic elastic constants of each phase. The individual phases were assumed to be elastically isotropic. The stress concentration factor in aluminium is less than unity in both samples, and it decreases with increasing stress, suggesting load transfer occurring to stiffer and stronger alumina and silicon throughout. Maximum longitudinal stress in alumina is almost double the applied stress in the sample under compression, and it is more than double the applied stress in

the sample under tension. Finally, at higher stresses in the sample under compression, longitudinal stress in alumina decreases owing to damage. No damage could be observed in the tensile sample by means of diffraction data.

Acknowledgements

The authors thank the synchrotron radiation facility BESSY (Berlin, Germany) for granting beamtime under proposal 2009_2_90335, and the EDDI beamline staff for their excellent technical assistance.

References

[1] Mortensen A, Llorca J. Annu Rev Mater Res 2010;40:243.
[2] Ashby MF. Acta Metall Mater 1993;41:1313.
[3] Prielipp H, Knechtel M, Clausen N, Streiffer SK, Müllejans H, Rühle M, et al. Mater Sci Eng A 1995;197:19.
[4] Sternitzke M, Knechtel M, Hoffmann M, Broszeit E, Rödel J. J Am Ceram Soc 1996;79:121.
[5] Feng HJ, Moore JJ. Metall Mater Trans. B 1995;26B:265.
[6] Liu W, Köster U. Mater Sci Eng A 1996;A210:1.
[7] Horvitz D, Gotman I, Gutmanas EY, Clausen N. J Eur Ceram Soc 2002;22:947.
[8] Xie X-Q, Zhang D, Fan T-x, Sakata T, Mori H, Okabe T, et al. Mater Lett 2002;56:102.
[9] San Marchi C, Kouzeli M, Rao R, Lewis JA, Dunand DC. Scripta Mater 2003;49:861.
[10] Waschkies T, Oberacker R, Hoffmann MJ. J Am Ceram Soc 2009;92:S79.
[11] Roy S, Butz B, Wanner A. Acta Mater 2010;58:2300.
[12] Launey ME, Munch E, Alsem DH, Saiz E, Tomsia AP, Ritchie RO. J Roy Soc Inter. doi: 10/1098/rsif.2009.0331.
[13] Garces G, Brunno G, Wanner A. Acta Mater 2007;55:5389.
[14] Daymond MR, Lund C, Bourke MAM, Dunand DC. Metall Mater Trans A 1999;30A:2989.
[15] Clausen B, Bourke MAM, Brown DW, Üstündag E. Mater Sci Eng A 2006;A421:9.
[16] Dutta M, Bruno G, Edwards L, Fitzpatrick ME. Acta Mater 2004;52:3881.
[17] Balch DK, Dunand DC. Acta Mater 2006;54:1501.
[18] Wanner A, Dunand DC. Metall Mater Trans A 2000;31A:2949.
[19] Wilkes TE, Harder BJ, Almer JD, Faber KT. Acta Mater 2009;57:6234.
[20] Young ML, Rao R, Almer JD, Haeffner DR, Lewis JA, Dunand DC. Acta Mater 2009;57:2362.
[21] Maire E, Owen A, Buffiere J-Y, Withers PJ. Acta Mater 2001;49:153.
[22] Roy S, Gibmeier J, Wanner A. Adv Eng Mater 2009;11:471.
[23] Newnham RE, Skinner DP, Cross LE. Mater Res Bull 1978;13:525.
[24] Huchler B, Staudenecker D, Weidler T, Mattern A, Nagel A, Kallien L, et al. In: Proceedings of symposium Verbundwerkstoffe und Werkstoffverbunde ,Frankfurt; 2005. p. 15.
[25] Genzel C, Denks IA, Gibmeier J, Klaus M, Wagener G. Nucl Instrum Methods Phys Res A 2007;578:23.
[26] Pyzalla A. J Nondestruct Evaluat 2000;19:21.
[27] Macherauch E, Müller P. Z Angewandte Physik 1961;13:305.
[28] ASM International Handbook Committee. Engineered materials handbook. Composites, vol. 1. Materials Park, OH: ASM International; 1987.
[29] Roy S, Wanner A. Compos Sci Technol 2008;68:1136.
[30] Weidenmann KA, Tavangar R, Weber L. Compos Sci Technol 2009;69:1660.
[31] Daymond MR. J Appl Phys 2004;96:4263.
[32] Withers PJ, Preuss M, Steuwer A, Pang JWL. J Appl Crystallogr 2007;40:891.
[33] Arsenault RJ, Taya M. Acta Metall 1987;35:651.
[34] Shackleford JF, Alexander W. Materials science and engineering handbook. Boca Raton, FL: CRC Press; 2001.
[35] ASM Handbook. Mechanical testing and evaluation, vol. 8. Materials Park, OH, USA: ASM International; 1985.
[36] Clausen B, Lorentzen T, Leffers T. Acta Mater 1998;46:3087.
[37] Dieter GE. Mechanical metallurgy. Maidenhead: McGraw-Hill; 1988.
[38] Gieske JH, Barsch JR. Phys Status Solidi 1968;29:121.
[39] Thomas JF. Phys Rev 1968;175:955.
[40] McSkimmin HJ, Andreatch P. J Appl Phys 1964;35:2161.